Available online at www.sciencedirect.com
ScienceDirect
Trans. Nonferrous Met. Soc. China 28(2018) 2274−2286
Transactions of Nonferrous Metals Society of China
www.tnmsc.cn

Discharge performance of Mg−Al−Pb−La anode for Mg−air battery

Yan FENG, Ge LEI, Yu-qing HE, Ri-chu WANG, Xiao-feng WANG

School of Materials Science and Engineering, Central South University, Changsha 410083, China

Received 8 October 2017; accepted 10 January 2018

Abstract: The discharge performance of Mg−Al−Pb−La anode was investigated by electrochemical techniques and compared with that of Mg−Al−Pb alloy. The results indicate that the Mg−Al−Pb−La anode provides enhanced corrosion resistance at open circle potential, and exhibits better discharge activity than the Mg−Al−Pb alloy. The utilization efficiency of Mg−Al−Pb−La anode is higher than that of commercial Mg−Al−Zn (AZ) and Mg−Al−Mn (AM) alloys. A single Mg−air battery with Mg−Al−Pb−La alloy as the anode and air as the cathode has an average discharge potential of 1.295 V and a discharge capacity of 1370 mA·h/g during discharge at 10 mA/cm^2, which is higher than that of batteries using Mg−Li anodes. The enhancement in discharge performance of the Mg−Al−Pb−La anode is caused by its modified microstructure, which reduces the self-corrosion and accelerates the spalling of oxidation products during battery discharge. Furthermore, the dissolution mechanism of Mg−Al−Pb−La anode during the discharge process was analyzed.

Key words: Mg−air battery; Mg−Al−Pb−La alloy; corrosion resistance; discharge activity; utilization efficiency

1 Introduction

Metal−air batteries provide higher theoretical energy density and lower cost than lithium-ion or alkaline batteries, thus attracting much attention for submarine, electromotive, emergency, and standby power applications [1−3]. In general, a metal−air battery is composed of an active metal anode, an air cathode and a saline electrolyte. During the discharge process, an anode metal is oxidized to produce electrons, while O_2 is reduced to OH^- by reaction with H_2O and electrons at the opposite air cathode [4,5]. The Mg−air battery is a promising electrochemical energy storage and conversion device since Mg has a negative standard electrode potential (−2.37 V (vs SHE)), a higher faradic capacity (2.2 A·h/g), a lower density (1.74 g/cm^3) and is abundant on the earth [6]. Among the metal−air batteries, the Mg−air battery has a high theoretical cell voltage (3.1 V), and a higher specific energy density (6.8 W·h/kg) than the Zn-air battery (1.3 W·h/kg) [7]. However, high polarization and low coulombic efficiency in practical use adversely affect the discharge performance of Mg anodes, thereby making the Mg−air battery less attractive than Al−air and Zn−air batteries. Firstly, the electrode surface of magnesium is normally covered by a film of discharge product $Mg(OH)_2$ that reduces the reaction area and shifts the potential of magnesium to a significantly less-negative value and thus affecting polarization [8]. A theoretical calculation using density functional theory proves that the potential shift of magnesium is dictated by the adsorption of hydroxide onto the magnesium surface. Moreover, suppressing the corrosion of magnesium will not significantly increase the available potential of the Mg−air battery [9]. Secondly, a magnesium electrode suffers severe self-discharge under both storage and discharge conditions. This side reaction promotes the evolution of hydrogen and wastefully consumes the metal, thus decreasing the coulombic efficiency of the Mg−air battery [10].

Alloying Mg with other metals effectively enhances its anode performance [11]. Mg−Al−Pb series alloys such as AP65 (Mg−6%Al−5%Pb) are good anode materials for high-power batteries, because the activated elements aluminum and lead accelerate the spalling of the discharge-products film and synergistically enhance the discharge activity of pure magnesium [12−14]. However, Mg−Al−Pb alloys are not stable at the open circuit potentials (OCP), and a small current density

Foundation item: Project (2015JC3004) supported by the Science and Technology Plan of Hunan Province, China; Project (2016JJ2147) supported by the Natural Science Foundation of Hunan Province, China; Project (51401243) supported by the National Natural Science Foundation of China

Corresponding author: Xiao-feng WANG; Tel/Fax: +86-731-88836638; E-mail: 209130@csu.edu.cn

DOI: 10.1016/S1003-6326(18)64872-1

results in the detachment of large metallic pieces. As a result, these alloys exhibit low anodic efficiencies when employed as anodes for Mg−air batteries discharged at current densities lower than 20 mA/cm^2 [4]. Rare earth elements (REs) can promote the degassing and purification processes in magnesium alloys [15]. Additionally, REs refine the microstructure of Mg alloys and inhibit self-corrosion on the electrode surface [16]. Several rare earth elements favor the breakdown of the $Mg(OH)_2$ film and improve the electrochemical activity and peak power density of Mg−H_2O_2 semi-fuel cells [17]. Based on these considerations, lanthanum (La) was added to the Mg−Al−Pb alloy in this work to enhance the discharge performance of the Mg−air battery when discharging at low current densities. Moreover, the dissolution mechanisms of Mg−Al−Pb−La alloys during discharge were analyzed.

2 Experimental

2.1 Preparation of materials

The Mg−Al−Pb and Mg−Al−Pb−La alloys with chemical compositions shown in Table 1, were prepared by melting ingots of pure magnesium (99.99%, mass fraction), aluminum (99.99%, mass fraction), lead (99.99%, mass fraction), and Zn (99.99%, mass fraction) together with Mg−18.5%La (mass fraction) and Al−19.8%Mn (mass fraction) master alloys in a resistance furnace at 1023 K under an argon atmosphere. The molten metal, protected by sulfur powder and argon, was poured into a water-cooled steel mold and cooled down to room temperature. The chemical compositions of the specimens were determined by inductively coupled plasma atomic emission spectrometry (ICP−AES), and the data indicated that the relative deviation of the content of each element was less than ±5%. The alloys were heat-treated at 603 K for 16 h, held at 693 K for 2 h, and then water-quenched to room temperature. The heat-treated alloys were selected as the research subjects for evaluating their discharge performance.

Table 1 Chemical compositions of Mg−Al−Pb and Mg−Al−Pb−La alloys determined by inductively coupled plasma atomic emission spectrometry (ICP−AES) (mass fraction, %)

Sample	Al	Pb	Zn	Mn	La	Mg
Mg−Al−Pb	6.052	5.121	0.101	0.051	0	Bal.
Mg−Al−Pb−La	6.131	4.883	0.098	0.048	1.021	Bal.

2.2 Microstructure characterization

Microstructures of the specimens were analyzed using optical microscopy and scanning electron microscopy. The compositions of the phases were detected using electron probe microscope analysis. The specimens used for metallographic observation were ground with SiC abrasive papers and polished with diamond grinding paste. A solution containing 1 mL nitric acid, 1 mL acetic acid, 1 g oxalic acid and 50−80 mL distilled water was used as the etchant to reveal the grain boundaries. The phase structures of Mg−Al−Pb and Mg−Al−Pb−La alloys were identified by an X-ray diffractometer using Cu K_α radiation from 10° to 80° with a scan speed of 4 (°)/min.

2.3 Electrochemical measurements

Electrochemical measurements of Mg−Al−Pb and Mg−Al−Pb−La alloys were carried out using a CHI660D electrochemistry workstation in a static 3.5% NaCl (mass fraction) solution at a constant temperature of 298 K. The electrolyte was prepared with deionized water. Specimens were polished with emery paper and buffed to a mirror finish with diamond grinding paste. Each specimen was sealed with epoxy resin except for an exposed surface of 10 mm × 10 mm, and subjected to the electrochemical tests in a three-electrode cell. A platinum sheet was used as the auxiliary electrode, a saturated calomel electrode with a standard electrode potential of 0.2412 V was used as reference electrode, and the sample to be tested was used as the working electrode.

The polarization curves were measured by sweeping the potential form −2.1 to −1.2 V at a scanning rate of 0.05 mV/s. Hydrogen evolution rates were measured by immersing the samples in a 3.5% NaCl solution at 298 K, using a flow-meter to collect hydrogen products of the reaction. A solution containing 200 g/L CrO_3 and 10 g/L $AgNO_3$ was used to remove the corrosion products after the samples were tested, and then the corroded surfaces of the samples were observed with a Quanta−200 SEM using secondary electron imaging. The potential−time curves in the course of galvanostatic discharge for 600 s were obtained by imposing anodic current densities of 10, 180, and 300 mA/cm^2. The electrochemical impedance spectra (EIS) were measured independently and recorded at the OCP after the samples were immersed in the electrolyte for 10 min. The scan frequency ranged from 1000 kHz to 0.01 Hz and the perturbation amplitude was 5 mV. The EIS data were then fitted with Zview software (Scribner Assoc., Inc.).

The utilization efficiency of each sample during the discharge process is given by the following relation [17]:

$$\eta = \frac{M_t}{M_a} \times 100\% \quad (1)$$

where η is the utilization efficiency (%), M_t is the theoretical mass loss (g) corresponding to the impressed current, and M_a is the actual mass loss (g) during the discharge period. The theoretical mass loss was calculated using Eq. (2) [5]:

$$M_t = \frac{It}{F\sum\left(\frac{X_i n_i}{m_i}\right)} \quad (2)$$

where I is the impressed current (A), t is the discharge time (s), F is the Faraday constant (96485 C/mol), and X_i, n_i, and m_i are the mass fraction, ionic valence, and molar mass (g/mol) of an alloying element, respectively. In Eq. (2), the numerator is the discharge passing through the testing sample, and the denominator is the theoretical electric quantity delivered by 1 g of testing sample. A solution of 200 g/L CrO_3 and 10 g/L $AgNO_3$ was also used to remove the discharge products after the test samples were discharged for a certain period. The actual mass loss was then obtained by subtracting the final mass of each sample from its initial mass. The discharge time at 10 mA/cm^2 was 10 h whereas that at 180 or 300 mA/cm^2 was 1 h, so as to achieve reasonable values of mass loss and thereby minimize the errors [17].

All electrochemical measurements were carried out three times in order to improve the experimental reliability.

2.4 Mg−air battery tests

The performance of prototype Mg−air batteries with Mg−Al−Pb and Mg−Al−Pb−La anodes was evaluated using a Neware battery testing system. The cathode was a home-made air electrode with a Pt/C catalyst and the electrolyte was 3.5% NaCl solution at 298 K. The anode and cathode have the same area of reaction surfaces; they were round and 1 cm in diameter. Figure 1 schematically shows the structure of a laboratory Mg−air battery [6]. The cell voltages provided by each anode at a current density of 10 mA/cm^2 were measured by galvanostatic discharge. The theoretical cycling life (C_L, h) of the magnesium anode can be predicted using Eq. (3):

$$C_L = \frac{\rho\pi r^2 d\eta Q_0}{3600\pi r^2 J} = \frac{\rho d\eta Q_0}{3600J} \quad (3)$$

where ρ is the density of anode material (g/cm^3), r is the radius of the electrode surface (1 cm), d is the thickness of the testing anode (0.5 cm), η is the anodic efficiency, Q_0 is the theoretical electric quantity provided by anode material (C/g), and J is the impressed current density (A/cm^2).

3 Results and discussion

3.1 Microstructure

Figure 2 shows the XRD patterns of the Mg−Al−Pb and Mg−Al−Pb−La alloys. The Mg−Al−Pb alloy exhibits α-Mg and β-$Mg_{17}Al_{12}$ phases, and the Mg−Al−Pb−La alloy mainly exhibits α-Mg and β-$Al_{11}La_3$ phases. Optical and back scattering (BS) images of Mg−Al−Pb and Mg−Al−Pb−La alloys are shown in Fig. 3. Electron probe microscope analyses of the second phases in Figs. 3(e) and (f) are described in Table 2. From Figs. 3(a), (c) and (e) it can be seen that two second phases are distributed discontinuously along the grain boundaries in the Mg−Al−Pb alloy. It can be deduced that the massive intergranular second phases are β-$Mg_{17}Al_{12}$ and Al_8Mn_5 compounds. However, the Al_8Mn_5 phase cannot be detected via XRD owing to the low content of manganese in the Mg−Al−Pb and Mg−Al−Pb−La alloys. Compared with the Mg−Al−Pb alloy, the Mg−Al−Pb−La alloy expressed a refined microstructure, as seen in Fig. 3(b). Three second phases can be seen in Mg−Al−Pb−La alloy, and all have small size with dispersive and homogeneous distributions. According to the XRD and EPMA results in Table 2, these second phases are acicular β-$Al_{11}La_3$, granulate Al_8Mn_5 and β-$Mg_{17}Al_{12}$ phases. This refining crystal behavior for rare earths in Mg alloys was observed in several prior studies [16]. The stronger binding force between Al and La atoms led to the formation of the

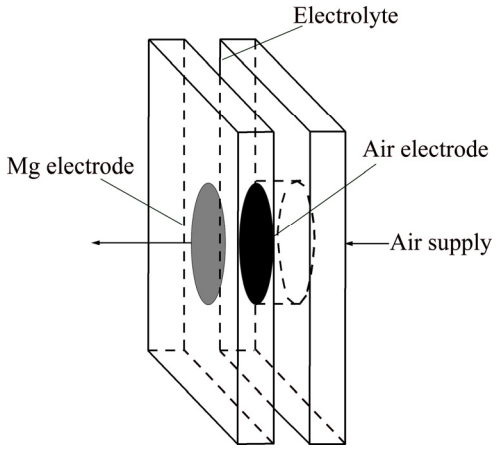

Fig. 1 Schematic of laboratory Mg−air battery

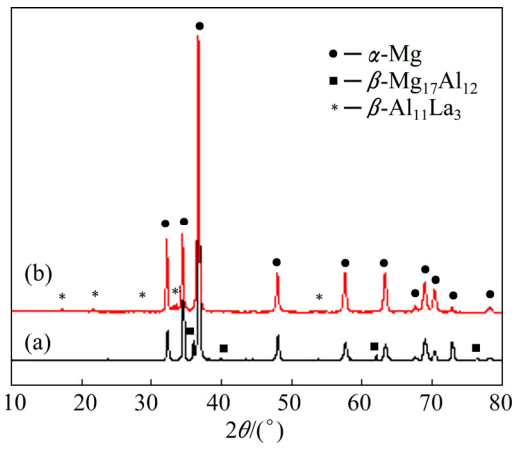

Fig. 2 XRD patterns of Mg−Al−Pb (a) and Mg−Al−Pb−La (b) alloys

β-$Al_{11}La_3$ phase, while restraining the formation of the β-$Mg_{17}Al_{12}$ phase in the Mg−Al−Pb−La alloy. Therefore, the amount of β-$Mg_{17}Al_{12}$ phase was so small that it cannot be detected via XRD in Mg−Al−Pb−La alloys.

From the EPMA data in Table 2, it can also be inferred that lead mainly existed in the form of a solid solution in the α-Mg matrix in Mg−Al−Pb and Mg−Al−Pb−La alloys. The lead in the Mg−Al−Pb alloy is distributed unevenly, this is confirmed by the non-uniform color of the α-Mg matrix. The bright areas (denoted by zone *B*) surrounding the intergranular $Mg_{17}Al_{12}$ phase in Fig. 3(e) were lead-rich areas with a

Table 2 Data of electron probe microscope analysis of Mg−Al−Pb and Mg−Al−Pb−La alloys

Sample	Point in Figs. 3(e) and (f)	Mole fraction/%						Phase
		Mg	Al	La	Pb	Zn	Mn	
Mg−Al−Pb	*A*	1.90	61.44	−	−	−	36.66	Al_8Mn_5
	B	80.79	7.51	−	10.66	1.04	−	α-Mg
	C	90.85	7.52	−	1.49	0.41	−	α-Mg
	D	61.90	36.15	−	−	1.95	−	β-$Mg_{17}Al_{12}$
Mg−Al−Pb−La	*E*	62.64	29.15	7.07	0.16	0.99	−	β-$Al_{11}La_3$
	F	59.14	37.25	3.36	0.12	0.13	−	β-$Mg_{17}Al_{12}$
	G	38.27	45.71	4.08	0.14	0.12	11.68	Al_8Mn_5
	H	90.05	501	0.03	3.11	0.62	0.08	α-Mg

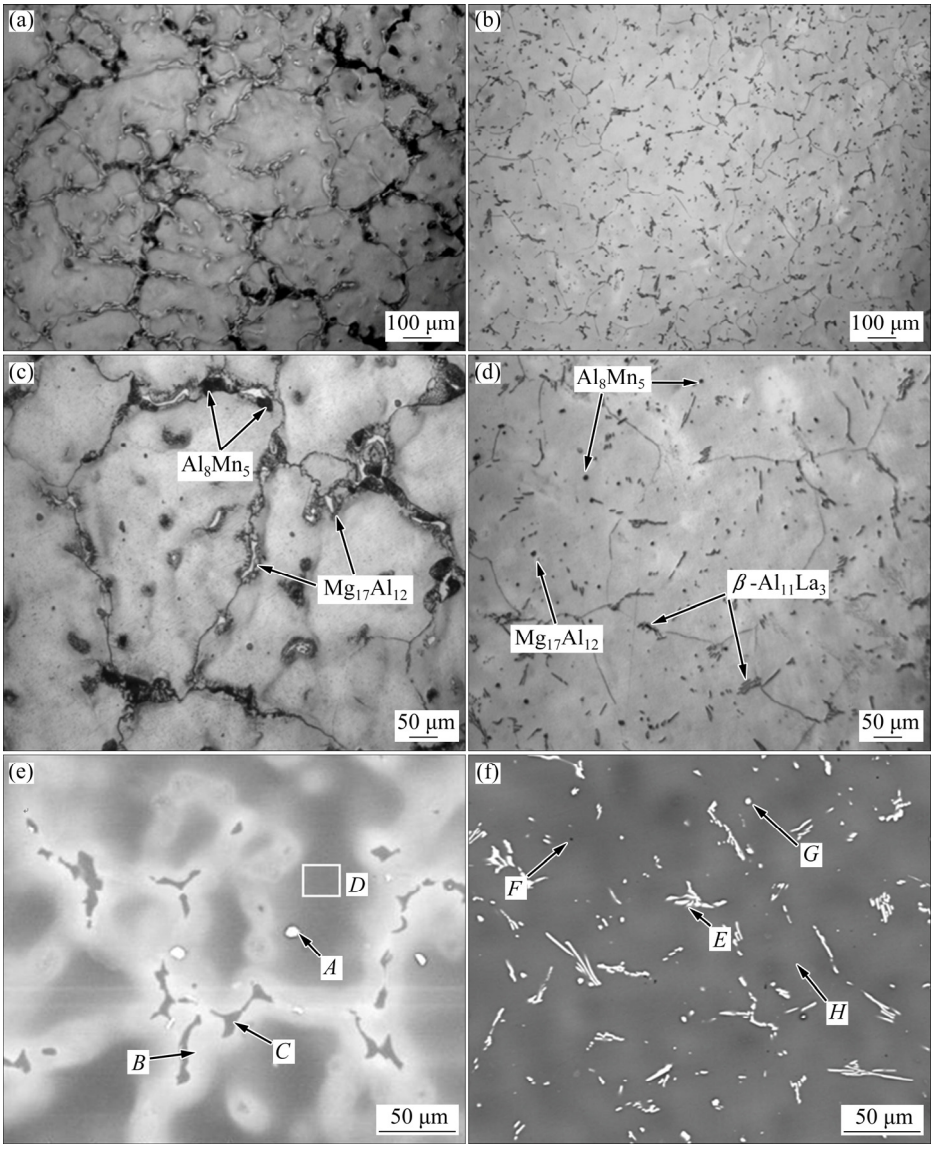

Fig. 3 Optical and back scattering (BS) images of samples: (a, c, e) Mg−Al−Pb alloy; (b, d, f) Mg−Al−Pb−La alloy

Pb content of 10.66% (mass fraction), while the dark areas (denoted by zone *C*) inside the magnesium were Pb-poor areas with a Pb content of only 1.49% (mass fraction). By contrast, the distribution of Pb element was relatively uniform in the Mg−Al−Pb−La alloy, as demonstrated by the homogeneous color in Fig. 3(f). From Table 2, it can be seen that Al and La existed in the form of β-$Mg_{17}Al_{12}$, β-$Al_{11}La_3$ and Al_8Mn_5 phases in the Mg−Al−Pb and Mg−Al−Pb−La alloys. Zn was mainly distributed in second phases, such as the β-$Mg_{17}Al_{12}$ phase in Mg−Al−Pb alloy and β-$Al_{11}La_3$ phase in Mg−Al−Pb−La alloy. Mn mainly existed in the Al_8Mn_5 phase.

3.2 Polarization curves and hydrogen evolution curves

Figure 4 shows the polarization curves of the Mg−Al−Pb and Mg−Al−Pb−La alloys in a 3.5% NaCl solution. It is important to note that *R*-correction has been performed in the polarization curves according to the equation $V_{true}=V-IR_s$ (where I is the measured potentiostatic current, R_s is the solution resistance obtained from EIS, V is the experimental applied potentiostatic potential, and V_{true} is the *IR*-corrected potential [18]. It can be seen that the addition of La does not shift the corrosion potential of Mg−Al−Pb alloy; this result is different from what has been reported in several prior studies concerning other rare-earth magnesium alloys [19]. The two samples exhibited nearly identical linear regions in their anodic branches below −1.54 V (vs SCE), while their cathodic polarization curves were somewhat different. The cathodic current densities of the Mg−Al−Pb−La alloy decreased more quickly with an increase of the applied potential at the cathodic branch, indicating that its hydrogen evolution rate was slower than that of the Mg−Al−Pb alloy.

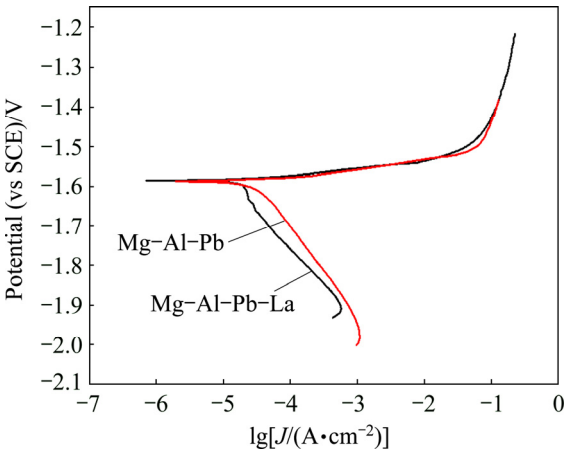

Fig. 4 Polarization curves of Mg−Al−Pb and Mg−Al−Pb−La alloys in 3.5% NaCl solution at 298 K

The curves shown in Fig. 4 were used to evaluate the corrosion current densities by extrapolating the cathodic branches back to the corrosion potentials. The potential range used for the Tafel extrapolation is 120−250 mV more negative than the corrosion potential [20]. The corrosion parameters derived from these polarization curves are listed in Table 3. According to Fig. 4 and Table 3, it is obvious that the addition of La significantly reduces the corrosion current density of Mg−Al−Pb alloy and improves its corrosion resistance at OCP. The corrosion density (J_{corr}) in the Mg−Al−Pb−La alloy was (10.0±0.9) μA/cm^2, which is lower than that of pure Mg [6], AZ31 [6] or Mg−Al−Pb−In alloys [5]; and it is equivalent to that of Mg−Al−Pb−Ce−Y alloy [6]. Even though the corrosion current densities may not give the accurate corrosion rate for many magnesium alloys, it is still acceptable to qualitatively deduce the corrosion rates using the corrosion current density. Mg−Al−Pb−La alloys with smaller corrosion current density exhibited better corrosion resistance. From Table 3, it can also be seen that the cathodic Tafel slope (b_c) of Mg−Al−Pb alloy is more negative than that of Mg−Al−Pb−La alloy. The cathodic Tafel slope values reflect the rate of the cathodic hydrogen evolution reaction. A more negative cathodic Tafel slope indicates a rapid cathodic hydrogen evolution reaction, which demonstrates rapid self-corrosion of magnesium alloys. Therefore, the Mg−Al−Pb alloy has a larger hydrogen evolution rate than the Mg−Al−Pb−La alloy. La changes the hydrogen evolution behavior during cathodic polarization although it barely affects the corrosion potential (φ_{corr}) of the Mg−Al−Pb alloy. Furthermore, the hydrogen evolution curves of

Table 3 Electrochemical corrosion parameters of Mg−Al−Pb and Mg−Al−Pb−La alloys evaluated from polarization curves

Sample	J_{corr}/ (μA·cm^{-2})	φ_{corr} (vs SCE)/ V	b_c/ (mV·dec^{-1})	v_{H_2} / (mL·cm^{-2}·h^{-1})
Mg−Al−Pb (this work)	30.4 ±1.2	−1.587	−222.2	2.80±0.12
Mg−Al−Pb−La (this work)	10.0±0.9	−1.585	−173.4	0.47±0.05
Pure Mg [6]	59.3±0.5	−1.755	−250.0	−
AZ31 [6]	23.6±2.0	−1.671	−207.0	−
Mg−Al−Pb−In [5]	35.4±7.0	−1.537	−194.0	−
Mg−Al−Pb−Ce−Y [6]	9.9±0.7	−1.616	−224.0	−

Mg−Al−Pb and Mg−Al−Pb−La alloys in a 3.5% NaCl solution were tested. The mean hydrogen evolution rates (v_{H_2}) are calculated and shown in Table 3. It can be seen that the mean hydrogen evolution rate decreased from (2.80±0.12) to (0.47±0.05) mL/(cm^2·h) with the addition of La to the Mg−Al−Pb alloy. It can be deduced that the addition of La to Mg−Al−Pb alloys restrains the evolution of hydrogen during the cathodic polarization process. This result is consistent with the results of WANG et al [15], who found that the corrosion product of Mg−La alloys easily deposits on the active site of the cathodic reaction and impedes the cathodic hydrogen evolution reaction. The Mg−Al−Pb−La alloy with a smaller hydrogen evolution rate exhibits better corrosion resistance at OCP than the Mg−Al−Pb alloy, which is consistent with the result of corrosion current densities calculated from polarization curves tests.

In general, the corrosion behavior and corrosion resistances of magnesium alloys are closely related to their compositions and microstructure features [21]. In Mg−Al−Pb alloys, the uneven distribution of lead in the magnesium matrix promotes self-corrosion. Moreover, the β-$Mg_{17}Al_{12}$ phase at the grain boundaries (Fig. 3(c)) serves as a galvanic cathode to accelerate the corrosion of α-Mg. Therefore, the Mg−Al−Pb alloy exhibits a larger corrosion current density and hydrogen evolution rate compared with other magnesium electrodes [5]. Doping Mg−Al−Pb alloy with La decreased the fraction of β-$Mg_{17}Al_{12}$ phase and facilitated the formation of β-$Al_{11}La_3$ phase. As reported in Ref. [22], the potential difference between α-Mg and the β-$Mg_{17}Al_{12}$ phases was 460 mV, while the potential difference between α-Mg and the Al−La phase was 8 mV. It can be deduced that the β-$Al_{11}La_3$ phase expressed weak cathodic properties in the micro-galvanic couples in the Mg−Al−Pb−La alloy. Moreover, the addition of La favored the uniform distribution of alloying elements in the Mg−Al−Pb alloy. Therefore, the micro-galvanic couple in Mg−Al−Pb−La alloy was inhibited, resulting in an enhancement of the corrosion resistance at OCP.

This interpretation is also confirmed by the secondary electron (SE) images in Fig. 5. The Mg−Al−Pb alloy suffered severe attack with a large number of pits distributed on the alloy surface after hydrogen evolution tests for 50 s (Figs. 5(a) and (b)). However, the Mg−Al−Pb−La alloy suffered only a weak attack with some small, shallow pits distributed on the alloy surface after the same tests (Figs. 5(c) and (d)). The magnified image in Fig. 5(b) shows that these pits in the Mg−Al−Pb alloy appear in the vicinity of the cathodic

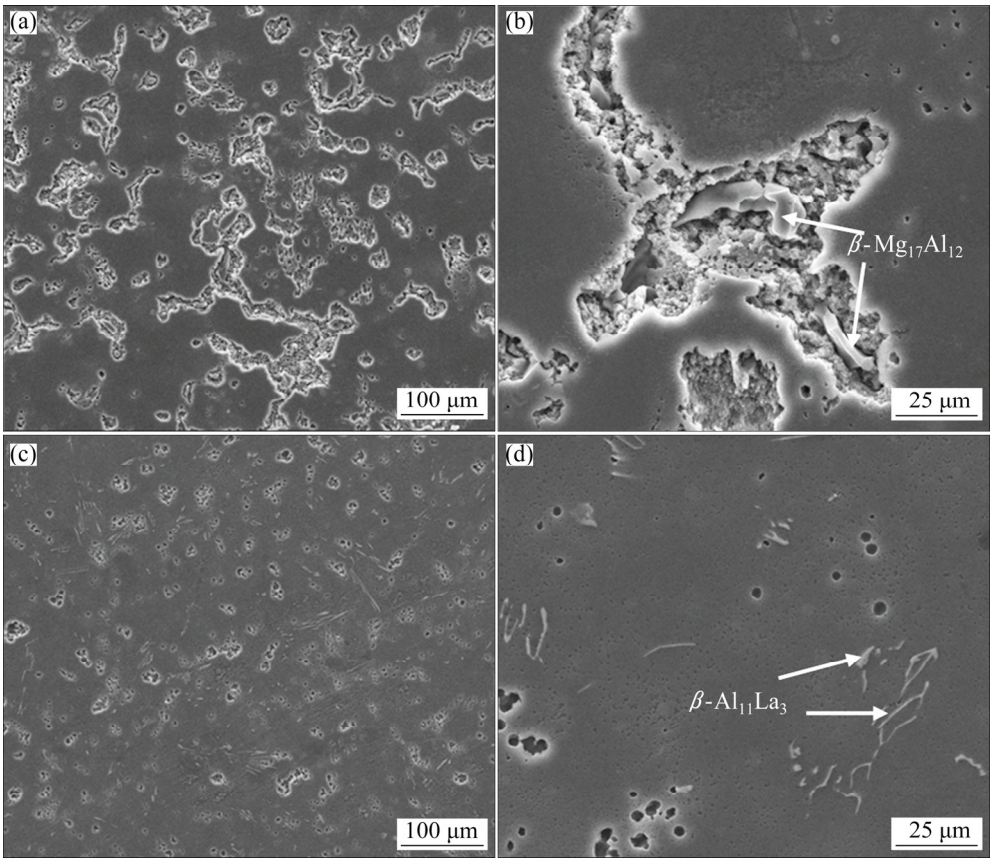

Fig. 5 Secondary electron (SE) images of Mg−Al−Pb and Mg−Al−Pb−La alloys during hydrogen evolution tests for 50 s in 3.5% NaCl solution at 298 K after removing corrosion products: (a) Mg−Al−Pb alloy; (b) Closed-up view of (a); (c) Mg−Al−Pb−La alloy; (d) Closed-up view of (c)

β-$Mg_{17}Al_{12}$ phase, which effectively initiates the pitting corrosion of the Mg matrix. Moreover, these pits are irregular and rough, demonstrating that metallic particles are stripped from the electrode surface. This kind of crystallographic corrosion is consistent with the results reported by WANG et al [5]. In contrast, a large number of round and clean pits can be observed on the corroded surface of the Mg−Al−Pb−La alloy under the same test conditions, as seen in Fig. 5(d). These round pores related to pitting corrosion were not caused by the detachment of grains, but rather by active dissolution [5]. These pit pores are not found in the vicinity of the β-$Al_{11}La_3$ phase, confirming that the β-$Al_{11}La_3$ phase has a weak cathode effect. As a consequence, the addition of La changes the corrosion behavior and promotes the corrosion resistance of the Mg−Al−Pb alloy.

3.3 Potential−time curves

Figure 6 shows the potential−time curves of Mg−Al−Pb and Mg−Al−Pb−La alloys at different anodic current densities in a 3.5% NaCl solution. A small current density of 10 mA/cm^2 was adopted to investigate the discharge behavior of a magnesium anode used for a long-term low power application, whereas large current densities of 180 and 300 mA/cm^2 were chosen to examine the discharge performance of a magnesium alloy employed as the anode for a short-term, high-power battery system [23]. From Fig. 6, it can be seen that a large current density causes the average discharge potential of the magnesium anodes to shift in a positive direction. The average discharge potentials of the Mg−Al−Pb and Mg−Al−Pb−La alloys measured from the potential−time curves are listed in Table 4. The average discharge potentials of the Mg−Al−Pb−La alloy at current densities of 10, 180 and 300 mA/cm^2 are −1.789, −1.763 and −1.749 V (vs SCE), respectively. Thus, the Mg−Al−Pb−La alloy exhibits a more negative potential at each current density than either the Mg−Al−Pb alloy or pure Mg. Therefore, the addition of La improves the discharge activity of the Mg−Al−Pb alloy.

The excellent discharge activity of the Mg−Al−Pb−La alloy can be inferred from its corrosion surface after discharge. Figure 7 shows the surface morphologies of the Mg−Al−Pb and Mg−Al−Pb−La alloys discharged at 300 mA/cm^2 for 10 min after removing the corrosion products. According to Figs. 7(a) and (b), the corroded surface of the Mg−Al−Pb alloy was rugged, with some pits produced by spalling of metallic

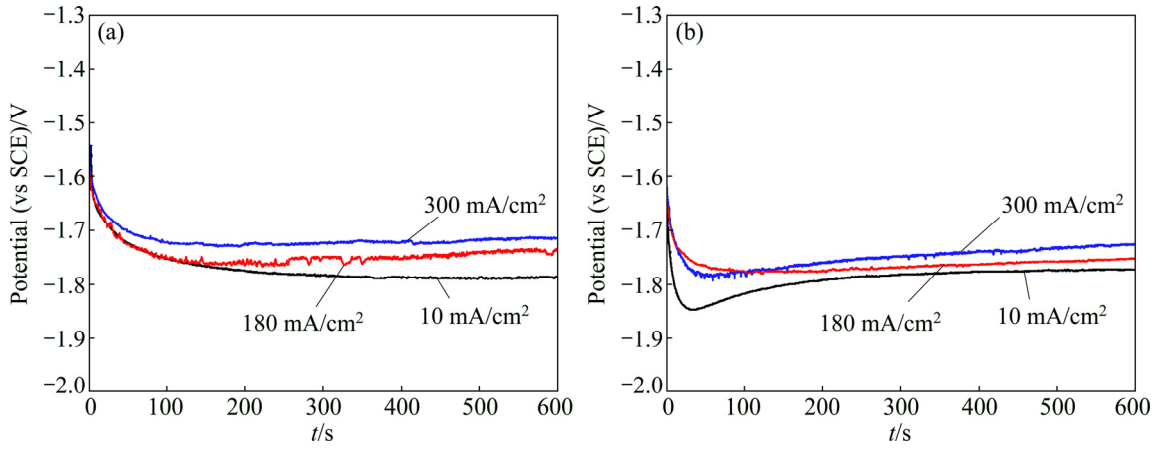

Fig. 6 Potential−time curves of Mg−Al−Pb (a) and Mg−Al−Pb−La (b) alloys at different anodic current densities in 3.5% NaCl solution at 298 K

Table 4 Electrochemical corrosion parameters of Mg−Al−Pb and Mg−Al−Pb−La alloys evaluated from galvanostatic curves

Sample	Average discharge potential (vs SCE)/V			Utilization efficiency, η/%		
	10 mA/cm^2	180 mA/cm^2	300 mA/cm^2	10 mA/cm^2 for 10 h	180 mA/m^2 for 1 h	300 mA/m^2 for 1 h
Mg−Al−Pb (this work)	−1.768	−1.744	−1.683	52.7±0.3	80.7±0.5	75.2±0.8
Mg−Al−Pb−La (this work)	−1.789	−1.763	−1.749	62.9±0.2	79.9±0.6	84.3±0.9
Pure Mg [6]	−1.649	−1.521	−1.422	55.6±0.1	64.0±0.5	62.2±0.5
AZ31 [6]	−	−	−	56.1±0.3	−	−
Mg−Al−Pb−In [5]	−1.798	−1.698	−1.433	41.4±1.1	87.7±0.9	83.3±0.5
Mg−Al−Pb−Ce−Y [6]	−	−	−	60.5±0.2	−	−

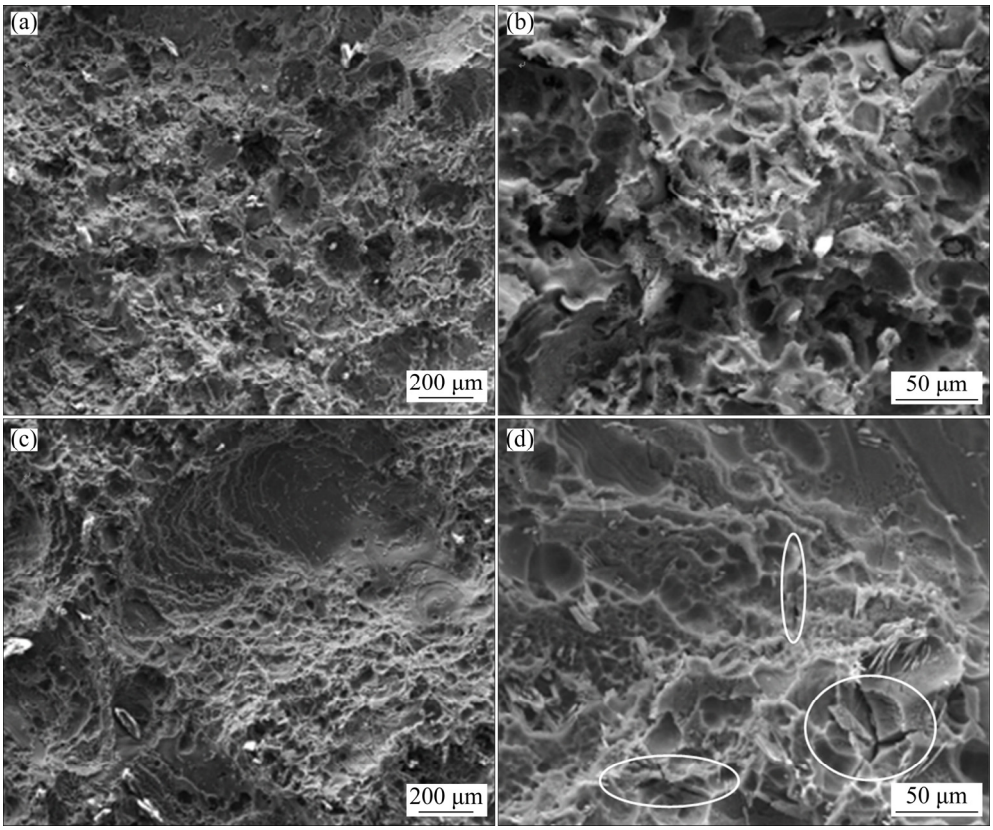

Fig. 7 Surface morphologies of Mg−Al−Pb and Mg−Al−Pb−La alloys discharged at 300 mA/cm^2 for 10 min after removing corrosion products: (a) Mg−Al−Pb alloy; (b) Closed-up view of (a); (c) Mg−Al−Pb−La alloy; (d) Closed-up view of (c)

particles; hence, it can be concluded that the active dissolution of the Mg−Al−Pb alloy was uneven. However, from Figs. 7(c) and (d), it can be seen that the Mg−Al−Pb−La alloy experienced uniform dissolution, and the corroded surface remained relatively smooth. The magnified image in Fig. 7(d) indicates that some cracks exist on the corroded surface of the Mg−Al−Pb−La alloy; thus, electrolyte can penetrate through to adequately contact the electrode surface, leading to an enhancement of the discharge activity.

Different discharge activities of Mg−Al−Pb and Mg−Al−Pb−La anodes can be explained by analyzing their compositions and microstructures. In Mg−Al−Pb series alloys, Pb and Al promote the breakdown of corrosion products in a synergistic mode [20]; consequently, these alloys exhibit better discharge activities than pure Mg or AZ series alloys. For the Mg−Al−Pb alloy, uneven distribution of the alloying elements results in localized dissolution, as confirmed by the corroded surface in Fig. 7(a). Moreover, FENG et al [6] claimed that it is clearly impossible for the β-$Mg_{17}Al_{12}$ phase in Mg−Al−Pb alloys to promote the active dissolution of the surrounding matrix. The discharge process in Mg−Al−Pb alloy is hindered, and it is different from the state of OCP because the anodic dissolution behavior of magnesium alloys depends on the applied current densities [24]. In the Mg−Al−Pb−La alloy, the discharge activity is improved for two reasons. Firstly, β-$Al_{11}La_3$ phase accelerates the active dissolution of the surrounding α-Mg matrix during discharge. The dispersive cathode β-$Al_{11}La_3$ phases form corrosion micro-couples with magnesium matrix, promoting the activation dissolution of the magnesium matrix. Figure 8 shows the surface morphology of Mg−Al−Pb−La alloy discharged at 300 mA/cm^2 for 10 s after removing the corrosion products. It can be seen that the α-Mg matrix around the β-$Al_{11}La_3$ phase exhibits prior dissolution, indicating that the β-$Al_{11}La_3$ phase accelerates the active dissolution of the surrounding α-Mg matrix during discharge, although it shows a weak cathode effect at OCP. The rapid dissolution of α-Mg around the β-$Al_{11}La_3$ phase causes high concentrations of Al^{3+} and Pb^{2+} ions, which can easily precipitate on the electrode surface and remove the oxidation products [25]. The activation reaction equations can be written as follows:

$$Mg = Mg^{2+} + 2e \quad (4)$$

$$2H_2O + 2e = H_2 + 2OH^- \quad (5)$$

$$Mg^{2+} + 2OH^- = Mg(OH)_2 \quad (6)$$

$$3Pb^{2+} + 8OH^- = Pb_3O_4 + 4H_2O \quad (7)$$

$$Al^{3+} + xMg(OH)_2 + 2OH^- + Cl^- = Mg_xAl(OH)_{2x+2}Cl \quad (8)$$

Thus, the β-$Al_{11}La_3$ phase improves the discharge activity of the Mg−Al−Pb−La alloy. Secondly, the uniform distribution of the β-$Al_{11}La_3$ phase accelerates the homogeneous dissolution of the magnesium matrix during discharge. Moreover, the addition of La refines the microstructure and promotes the composition uniformity of the Mg−Al−Pb alloy, which can be seen in Fig. 3. These effects improve the uniform dissolution of the magnesium matrix, as shown in Fig. 7(c). Thus, the discharge activity of the Mg−Al−Pb−La alloy is further improved.

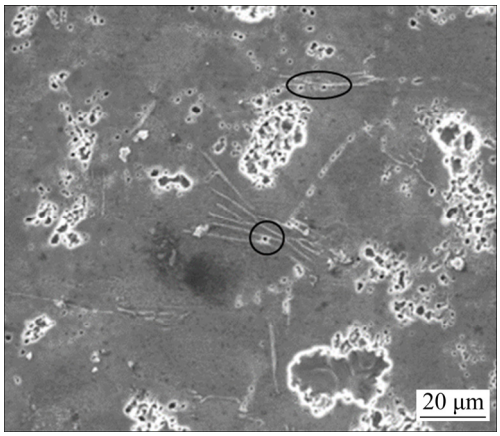

Fig. 8 Surface morphology of Mg−Al−Pb−La alloy discharged at 300 mA/cm^2 for 10 s after removing corrosion products

3.4 Utilization efficiency

The calculated utilization efficiencies of the Mg−Al−Pb and Mg−Al−Pb−La alloys are summarized in Table 4. It can be observed that an increase in anodic current densities from 10 to 300 mA/cm^2 leads to a significant enhancement in utilization efficiency for magnesium alloys. This is because a low current density promotes the chunk effect and accelerates the spalling of large metallic pieces [5]. According to Table 4, Mg−Al−Pb−La alloy possesses the highest utilization efficiency at current densities of 10 and 300 mA/cm^2 compared with other magnesium alloys, such as Mg−Al−Pb, Mg−Al−Pb−In, and Mg−Al−Pb−Ce−Y alloys. The utilization efficiency of the Mg−Al−Pb−La alloy at a current density of 10 mA/cm^2 reaches (62.9±0.2)%, which is higher than that of Mg−Al−Pb−Ce−Y alloy [6]. The utilization efficiency of the Mg−Al−Pb−La alloy at a current density of 300 mA/cm^2 reaches (84.3±0.9)%, which is higher than that of pure magnesium and is close to that (83.3±0.5)% of Mg−Al−Pb−In alloy [5]. The Mg−Al−Pb and Mg−Al−Pb−La alloys have nearly the same utilization efficiency, which are (80.7±0.5)% and (79.9±0.6)% at a current density of 180 mA/cm^2, respectively. Thus, La addition enhances the utilization efficiency of Mg−Al−Pb alloy in the course of the discharge.

During the discharge process, hydrogen evolution, self-corrosion, and grain detachment severely decrease the utilization efficiency of magnesium alloys. From the images of the corroded surface in Fig. 7, it can be deduced that the spalling of metallic particles occurs in the Mg−Al−Pb alloy, whereas active dissolution occurs in the Mg−Al−Pb−La alloy. The relatively uniform compositions in the Mg−Al−Pb−La alloy inhibit the self-peeling of large metallic particles. According to the polarization curves in Fig. 4, the cathodic curve of the Mg−Al−Pb−La alloy is on the left of that of the Mg−Al−Pb alloy when the potential is more negative than −1.6 V (vs SCE). It can be deduced that the Mg−Al−Pb−La alloy exhibits weak cathodic hydrogen evolution reaction at these discharge potentials (<−1.6 V (vs SCE)), showing an enhancement of the anodic utilization efficiency. Additionally, the refined grains in the Mg−Al−Pb−La alloy create more grain boundaries (Figs. 3(a) and (b)), playing a vital role in inhibiting gas evolution during discharge [26]. It can also be deduced that for the Mg−Al−Pb−La alloy, a higher utilization efficiency was obtained at a current density of 300 mA/cm^2 than at 10 mA/cm^2. A large current density can drastically change the surface condition of the working electrode and promote the general dissolution of the electrode. The magnesium alloy with a smaller corrosion current density might not always be more anti-corrosive during the discharge process; therefore, hydrogen evolution, self-corrosion, and grain detachment occur in the magnesium alloy with smaller corrosion current density and decrease the utilization efficiency.

3.5 Performance of Mg−air batteries

Prototype Mg−air batteries with Mg−Al−Pb and Mg−Al−Pb−La anodes were assembled to evaluate the discharge performance of these samples. Figure 9 shows the discharge curves of the Mg−air batteries at a current

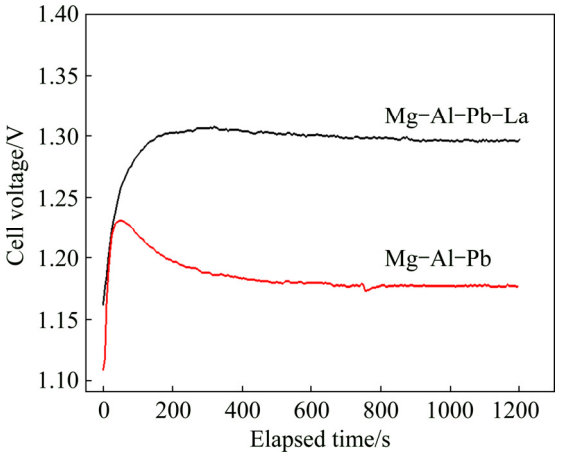

Fig. 9 Discharge curves of Mg−air batteries with Mg−Al−Pb and Mg−Al−Pb−La anodes in 3.5% NaCl solution at current density of 10 mA/cm^2

density of 10 mA/cm^2. The open circuit voltage (OCV) values together with the average voltages after discharging for 20 min are given in Table 5. From Table 5, the Mg−Al−Pb−La anode exhibits the highest average voltage of 1.295 V, followed by the Mg−Al−Pb−Ce−Y anode [6], indicating that both provide higher voltages than the Mg−Al−Pb (AP), Mg−Al−Zn (AZ), or Mg−Li anodes [27]. Therefore, Mg−Al−Pb−La alloy with strong discharge activity is valuable to offer high voltages when utilized as the anode for Mg−air batteries. The discharge capacities of Mg−air batteries were measured and are shown in Table 5. The discharge capacity of the Mg−air battery using Mg−Al−Pb−La anode is 1370 mA·h/kg, while that using Mg−Al−Pb anode is 1050 mA·h/kg.

The theoretical cycling life at each current density can be obtained based on the average value of utilization efficiencies using Eq. (3). According to Table 5, the Mg−Al−Pb anode exhibits shorter cycling life than pure Mg or AZ31 anodes at a current density of 10 mA/cm^2, while its cycling life is largely improved by the addition of La, becoming even longer than that of the Mg−Al−Pb−Ce−Y anode. The long cycling life at a given current density is achieved for the anode with high efficiency, as summarized in Table 5. Hence, improving the anodic efficiency is an effective approach to prolong the cycling life of a metal anode. Mg−Al−Pb−La anode with a long cycling life can suppress the side reactions during discharge, and thus is a good candidate for the anodes of Mg−air batteries. The correspondence between the anodic efficiency and cycling life also appears in Mg−Al−Pb−In anode [5]. According to Tables 4 and 5, the Mg−Al−Pb−In alloy exhibits the shortest cycling life as well as a lower anodic efficiency than other magnesium alloys at 10 mA/cm^2; while it exhibits the longest cycling life as well as the largest anodic efficiency at 180 mA/cm^2. Thus, the Mg−Al−Pb−In anode is suitable for discharge at a large current density, such as for high-power seawater batteries.

3.6 Electrochemical impedance spectra (EIS)

The EIS of Mg−Al−Pb and Mg−Al−Pb−La alloys in a 3.5% NaCl solution are shown in Fig. 10. These EIS, obtained at the OCP after the samples were soaked in the electrolyte for 10 min, give useful information about the corrosion in the initial stage. The inserted figure presented in Fig. 10(a) indicates that the Nyquist plot for the Mg−Al−Pb alloy shrinks to a significantly smaller dimension than that of the Mg−Al−Pb−La alloy. According to Fig. 10(a), the Nyquist plots for both Mg−Al−Pb and Mg−Al−Pb−La alloys consist of a large

Table 5 Discharge performances of Mg−air batteries with Mg−Al−Pb and Mg−Al−Pb−La anodes discharged for 20 min

Anode	OCV	Average voltage*/V	Cycling life /h		Discharge capacity*/ (mA·h·g^{-1})
			10 mA/cm^2	180 mA/cm^2	
Mg−Al−Pb	1.703	1.192	97.6	8.3	1050
Mg−Al−Pb−La	2.010	1.295	128.7	9.1	1370
Pure Mg [6]	2.096	1.069	106.3	6.8	−
AZ31 [6]	1.950	1.012	110.0	−	−
Mg−Al−Pb−In alloy [5]	−	−	84.67	10.0	−
Mg−Al−Pb−Ce−Y [6]	2.074	1.276	121.7	−	−

* Data were obtained at current density of 10 mA/cm^2

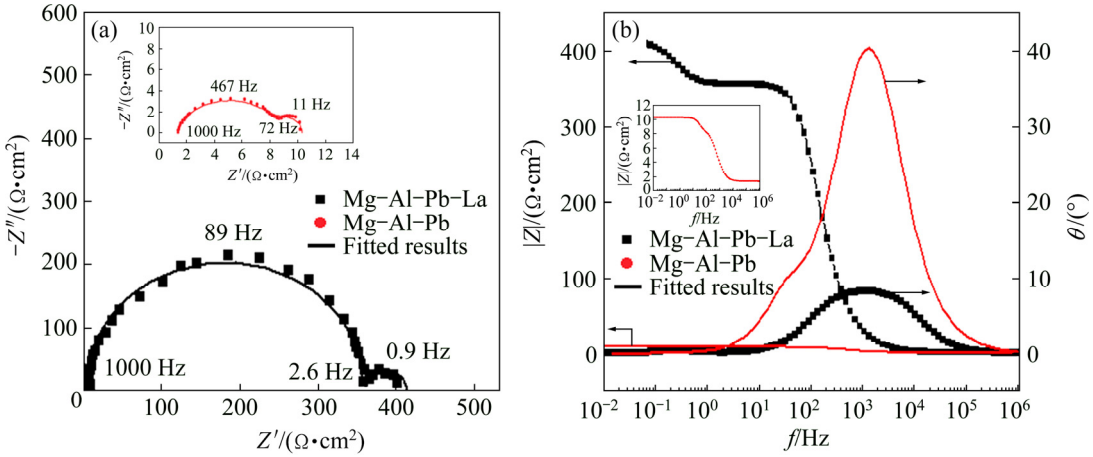

Fig. 10 Electrochemical impedance spectra (EIS) in Nyquist (a) and Bode (b) plots of Mg−Al−Pb and Mg−Al−Pb−La alloys in 3.5% NaCl solution at 298 K

capacitive loop in the high frequency region and a small capacitive loop in the low frequency range. The former is related to the charge transfer process and electric double layer at the electrode/electrolyte interface [28], whereas the latter is due to corrosion product film covering the electrode surface and/or the diffusion of electrolyte through this solid film [29]. The diameter of the large loop gives the charge transfer resistance while that of the small one is equal to the resistance of the corrosion product film. It can be observed that each loop for the Mg−Al−Pb−La alloy is larger than the corresponding one for the Mg−Al−Pb alloy, implying that the former exhibits higher corrosion resistance than the latter. The calculated values for the charge transfer resistance (R_t) and surface film resistance (R_f) are higher in the Mg−Al−Pb−La alloy than the corresponding values in Mg−Al−Pb alloy, implying that the Mg−Al−Pb−La alloy exhibits a lower corrosion rate than the Mg−Al−Pb alloy. The corrosion resistances of magnesium alloys deduced from EIS tests are consistent with the values deduced form the corrosion current densities and the hydrogen evolution rates summarized in Table 3. As seen in Table 3, the Mg−Al−Pb−La alloy has a corrosion current density of (10.0±0.9) μA/cm^2, which is smaller than that of the Mg−Al−Pb alloy; similarly, the hydrogen evolution rate of (0.47±0.05) mL/(cm^2·h) is also lower than that of the Mg−Al−Pb alloy.

The EIS plots of the Mg−Al−Pb and Mg−Al−Pb−La alloys are equivalent to the circuit shown in Fig. 11, which is the same as that of the Mg−Al−Pb−Ce−Y alloy [6]. In Fig. 11, R_s is the solution resistance, R_t and CPE_{dl} connected in parallel describe the high frequency capacitive loop. R_t is the charge transfer resistance, and CPE_{dl} is a constant phase element (CPE) used to substitute for the capacitor of an electric double layer (C_{dl}) owing to the nonhomogeneity of the electrochemical system [30]. The parallel connection of R_f and CPE_f, which denote the resistance and the constant phase element for the $Mg(OH)_2$ film, respectively, is adopted to characterize the low frequency capacitive loop. The CPE is defined and calculated by three parameters, Y, n and ω_m [5]. Y is often used as the capacitance of a corroding system, and has the dimension of $\Omega^{-1}\cdot cm^{-2}\cdot s^n$, in which n (varying from 0 to 1) is a dimensionless exponent. In both Mg−Al−Pb and Mg−Al−Pb−La alloys, n is equal to 1, indicating that the CPE is identical to a pure capacitor. ω_m is the frequency at which the imaginary part of the impedance has the maximum value. According to Table 6, Mg−Al−Pb−La alloy has much larger values of R_t and R_f than Mg−Al−Pb alloy; hence, the former dissolves more slowly at OCP than the latter, and the $Mg(OH)_2$ film protects the Mg−Al−Pb−La from further attack. This result is ascribed to the modification of rare earths, which promote the formation of protective film on the surface of magnesium alloys [19].

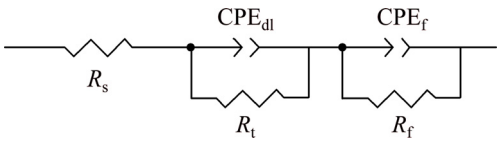

Fig. 11 Equivalent circuit of Mg−Al−Pb and Mg−Al−Pb−La alloys corresponding to EIS results

Table 6 Electrochemical parameters of Mg−Al−Pb and Mg−Al−Pb−La alloys obtained by fitting electrochemical impedance spectra

Magnesium alloy	R_s/ (Ω·cm^2)	R_t/ (Ω·cm^2)	Y_{dl}/ ($\Omega^{-1}\cdot cm^{-2}\cdot s^n$)	n_{dl}
Mg−Al−Pb	1.4	7.2	1.1×10^{-4}	1
Mg−Al−Pb−La	2.3	353.3	3.9×10^{-6}	1

Magnesium alloy	R_f/ (Ω·cm^2)	Y_f/ ($\Omega^{-1}\cdot cm^{-2}\cdot s^n$)	n_f
Mg−Al−Pb	1.8	2.4×10^{-3}	1
Mg−Al−Pb−La	57.2	1.2×10^{-2}	1

4 Conclusions

1) The Mg−Al−Pb−La anode exhibited an improved corrosion resistance at OCP and thus can be stored for long periods of time in the electrolyte. Moreover, this alloy had stronger discharge activity along with higher anodic efficiencies than other magnesium anodes when small current densities were applied.

2) The utilization efficiency of Mg−Al−Pb−La alloy at 10 mA/cm^2 reached (62.9±0.2)%, which is significantly higher than those of commercial AZ and AM series magnesium alloys.

3) The enhanced discharge performance of the Mg−Al−Pb−La alloy was attributed to its modified microstructure. The refined crystal grains with relatively uniform composition in the matrix promoted uniform dissolution of the anode during discharge, thereby suppressing the detachment of large metallic particles and improving the anodic efficiency. The dispersed β-$Al_{11}La_3$ phase with small grain size decreased the driving force of micro-galvanic corrosion in the Mg−Al−Pb−La alloy, and favored the formation of a protective $Mg(OH)_2$ film on the alloy surface at OCP. Thus, the corrosion resistance of this alloy was largely improved in the unloaded condition. Meanwhile, the β-$Al_{11}La_3$ phase accelerated the active dissolution of the surrounding matrix during discharge, which boosted the self-peeling of oxidation products and accelerated the discharge activity of the Mg−Al−Pb−La alloy. All these

aspects are responsible for the desirable performance of the Mg−Al−Pb−La alloy.

References

[1] FAN Liang, LU Hui-min, LENG Jing. Performance of fine structured aluminum anodes in neutral and alkaline electrolytes for Al−air batteries [J]. Electrochimca Acta, 2015, 165: 22−28.

[2] MA Jing-ling, WEN Jiu-ba, GAO Jun-wei, LI Quan-an. Performance of Al−0.5Mg−0.02Ga−0.1Sn−0.5Mn as anode for Al−air battery in NaCl solutions [J]. Journal of Power Sources, 2014, 253: 419−423.

[3] ALEXANDER K, YAIR E E. The impact of nano-scaled materials on advanced metal–air battery systems [J]. Nano Energy, 2013, 2: 468−480.

[4] ZHANG Tian-ran, TAO Zhan-liang, CHEN Jun. Magnesium−air batteries: From principle to application [J]. Materials Horizons, 2014, 1: 196−206.

[5] WANG Nai-guang, WANG Ri-chu, PENG Chao-qun, PENG Bing, FENG Yan, HU Cheng-wang. Discharge behaviour of Mg−Al−Pb and Mg−Al−Pb−In alloys as anodes for Mg−air battery [J]. Electrochimca Acta, 2014, 149: 193−205.

[6] FENG Yan, XIONG Wen-hui, ZHANG Jun-chang, WANG Ri-chu, WANG Nai-guang. Electrochemical discharge performance of Mg−Al−Pb−Ce−Y alloy as anode for Mg−air battery [J]. Journal of Materials Chemistry A, 2016, 22: 8658−8668.

[7] LEE J S, SUN T K, CAO R G, CHOI N S, LIU M L, LEE K T, CHO J P. Metal−air batteries: Metal–air batteries with high energy density: Li–air versus Zn–air [J]. Advanced Energy Materials, 2011, 1: 34−50.

[8] LV Yao-zhuo, LIU Min, XU Yan, CAO Dian-xue, FENG Jing. The electrochemical behaviors of Mg−8Li−3Al−0.5Zn and Mg−8Li−3Al−1.0Zn in sodium chloride solution [J]. Journal of Power Sources, 2013, 225: 124−128.

[9] YUASA M, HUANG X S, SUZUKI K, MABUCHI M, CHINO Y. Discharge properties of Mg−Al−Mn−Ca and Mg−Al−Mn alloys as anode materials for primary magnesium−air batteries [J]. Journal of Power Sources, 2015, 297: 449−456.

[10] CHEN L D, NØRSKOW J K, LUNTZ A C. Theoretical limits to the anode potential in aqueous Mg−air batteries [J]. Journal of Physical Chemistry C, 2015, 119: 19660−19667.

[11] CAO Dian-xue, WU Lin, WANG Gui-ling, LV Yao-zhuo. Electrochemical oxidation behavior of Mg−Li−Al−Ce−Zn and Mg−Li−Al−Ce−Zn−Mn in sodium chloride solution [J]. Journal of Power Sources, 2008, 183: 799−804.

[12] FENG Yan, WANG Ri-chu, PENG Chao-qun. Researches and applications of magnesium anode materials in seawater battery [J]. Transactions of Nonferrous Metals Society of China, 2011, 21: 259−268.

[13] WANG Nai-guang, WANG Ri-chu, PENG Chao-qun, FENG Yan. Enhancement of the discharge performance of AP65 magnesium alloy anodes by hot extrusion [J]. Corrosion Science, 2014, 81: 85−95.

[14] WEN Li, YU Kun, XIONG Han-qing, DAI Yi-long, YANG Shi-hai, QIAO Xue-yan, TENG Fei, FAN Su-feng. Composition optimization and electrochemical properties of Mg−Al−Pb−(Zn) alloys as anodes for seawater activated battery [J]. Electrochimica Acta, 2016, 194: 40−51.

[15] WANG Nai-guang, WANG Ri-chu, PENG Chao-qun, FENG Yan, CHEN Bin. Effect of hot rolling and subsequent annealing on electrochemical discharge behavior of AP65 magnesium alloy as anode for seawater activated battery [J]. Corrosion Science, 2012, 64: 17−27.

[16] SUDHOLZ A D, GUSIEVA K, CHEN X B, MUDDLE B C, GIBSON M A, BIRBILIS N. Electrochemical behavior and corrosion of Mg−Y alloys [J]. Corrosion Science, 2011, 53: 2277−2282.

[17] FENG Yan, LIU Li, WANG Ri-chu, PENG Chao-qun, WANG Nai-guang. Microstructure and electrochemical corrosion properties of Mg−Al−Pb and Mg−Al−Pb−Ce anode materials [J]. Transactions of Nonferrous Metals Society of China, 2016, 26: 1379−1387.

[18] LV Yan-zhuo, XU Yan, CAO Dian-xue. The electrochemical behaviors of Mg, Mg−Li−Al−Ce and Mg−Li−Al−Ce−Y in sodium chloride solution [J]. Journal of Power Sources, 2011, 196: 8809−8814.

[19] SONG G L, UNOCIC K A. The anodic surface film and hydrogen evolution on Mg [J]. Corrosion Science, 2015, 98: 758−765.

[20] PINTO R M, FERREIRA M G S, CARMEZIM M J, MONTEMOR M F. The corrosion behavior of rare-earth containing magnesium alloys in borate buffer solution [J]. Electrochimica Acta, 2011, 56: 1535−1545.

[21] YAO Yu-fen, CHEN Chang-guo, LIU Yu-ping, SI Yu-jun. Effect of lanthanum salt on electrochemical behavior of AZ31 magnesium alloy [J]. Journal of the Chinese Society of Rare Earths, 2009, 27: 688−695.

[22] YU Kun, XIONG Han-qing, WEN Li, DAI Yi-long, YANG Shi-hai, FAN Su-feng, TENG Fei, QIAO Xue-yan. Discharge behavior and electrochemical properties of Mg-Al-Sn alloy anode for seawater activated battery [J]. Transactions of Nonferrous Metals Society of China, 2015, 25: 1234−1240.

[23] LIU Wen-juan, CAO Fa-he, CHEN An-na, CHANG Lin-rong, ZHANG Jian-qing, CAO Chu-nan. Corrosion behavior of AM60 magnesium alloys containing Ce or La under thin electrolyte layers. Part 1: Microstructural characterization and electrochemical behavior [J]. Corrosion Science, 2010, 52: 627−638.

[24] ZHAO Jun, YU Kun, HU Ya-nan, LI Shao-jun, TAN Xin, CHEN Fu-wen, YU Zhi-ming. Discharge behavior of Mg−4wt%Ga−2wt%Hg alloy as anode for seawater activated battery [J]. Electrochimica Acta, 2011, 56: 8224−8231.

[25] SONG G L, ATRENS A, DARGUSCH M. Influence of microstructure on the corrosion of diecast AZ80D [J]. Corrosion Science, 1999, 41: 249−273.

[26] WANG Nai-guang, WANG Ri-chu, PENG Chao-qun, FENG Yan, ZHANG Xiang-yu. Influence of aluminum and lead on activation of magnesium as anode [J]. Transactions of Nonferrous Metals Society of China, 2010, 20: 1403−1411.

[27] MA Yi-bin, LI Ning, LI De-yu, ZHANG Mi-lin, HUANG Xiao-mei. Performance of Mg−14Li−1Al−0.1Ce as anode for Mg−air battery [J]. Journal of Power Sources, 2011, 196: 2346−2350.

[28] HUANG Guang-sheng, ZHAO Yan-chun, WANG Yan-xia, ZHANG Hua, PAN Fu-sheng. Performance of Mg–air battery based on AZ31 alloy sheet with twins [J]. Materials Letters, 2013, 113: 46−49.

[29] UDHAYAN R, BHATT D P. On the corrosion behavior of magnesium and its alloys using electrochemical techniques [J]. Journal of Power Sources, 1996, 63: 103−107.

[30] SONG Ying-wei, SHAN Da-yong, CHEN Rong-shi, HAN En-hou. Corrosion characterization of Mg−8Li alloy in NaCl solution [J]. Corrosion Science, 2009, 51: 1087−1094.

镁空气电池阳极 Mg−Al−Pb−La 合金的放电行为

冯 艳，雷 格，贺玉卿，王日初，王小锋

中南大学 材料科学与工程学院，长沙 410083

摘 要：通过电化学技术分析镁空气电池阳极 Mg−Al−Pb−La 合金的放电行为，并与 Mg−Al−Pb 合金的放电行为进行比较。结果表明，相对于 Mg−Al−Pb 合金，Mg−Al−Pb−La 合金在开路电位下耐蚀性增强，表现出更好的放电活性。Mg−Al−Pb−La 合金阳极的利用效率比商用 Mg−Al−Zn (AZ) 和 Mg−Al−Mn (AM)合金阳极的利用效率高。由 Mg−Al−Pb−La 阳极和空气阴极组成的单个镁空气电池的平均放电电压为 1.295 V，在放电电流密度为 10 mA/cm^2 时其放电容量为 1370 mA·h/g，比 Mg−Li 合金作为空气电池阳极时的放电容量高。Mg−Al−Pb−La 阳极放电性能的增强是由于显微组织的改变降低了自腐蚀，加速了电池放电过程中氧化产物的脱落。另外，分析了 Mg−Al−Pb−La 合金阳极在放电过程中的溶解机制。

关键词：镁空气电池；Mg−Al−Pb−La 合金；耐蚀性；放电活性；利用率

(Edited by Wei-ping CHEN)